Acta Crystallographica Section D
Biological Crystallography
ISSN 0907-4449

High-resolution structure of the p53 core domain: implications for binding small-molecule stabilizing compounds

William C. Ho,[a,b] Cheng Luo,[a] Kehao Zhao,[a] Xiaomei Chai,[a] Mary X. Fitzgerald[a] and Ronen Marmorstein[a,b]*

[a]The Wistar Institute, Philadelphia, PA 19104, USA, and [b]The University of Pennsylvania Department of Chemistry, Philadelphia, PA 19104, USA

Correspondence e-mail: marmor@wistar.org

Received 28 July 2006
Accepted 22 September 2006

PDB References: p53–Tris complex, 2ioi; p53–HEPES complex, ioo; p53–2-propanol complex, 2iom.

The p53 transcriptional regulator is the most frequently mutated protein in human cancers and the majority of tumor-derived p53 mutations map to the central DNA-binding core domain, with a subset of these mutations resulting in reduced p53 stability. Here, the 1.55 Å crystal structure of the mouse p53 core domain with a molecule of tris(hydroxymethyl)aminomethane (Tris) bound through multiple hydrogen bonds to a region of p53 shown to be important for repair of a subset of tumor-derived p53-stability mutations is reported. Consistent with the hypothesis that Tris binding stabilizes the p53 core domain, equilibrium denaturation experiments are presented that demonstrate that Tris binding increases the thermodynamic stability of the mouse p53 core domain by 3.1 kJ mol^{-1} and molecular-dynamic simulations are presented revealing an overall reduction in root-mean-square deviations of the core domain of 0.7 Å when Tris is bound. It is also shown that these crystals of the p53 core domain are suitable for the multiple-solvent crystal structure approach to identify other potential binding sites for possible core-domain stabilization compounds. Analysis of the residue-specific temperature factors of the high-resolution core-domain structure, coupled with a comparison with other core-domain structures, also reveals that the L1, H1–S5 and S7–S8 core-domain loops, also shown to mediate various p53 activities, harbor inherent flexibility, suggesting that these regions might be targets for other p53-stabilizing compounds. Together, these studies provide a molecular scaffold for the structure-based design of p53-stabilization compounds for development as possible therapeutic agents.

1. Introduction

The p53 tumor-suppressor protein is crucial in maintaining genomic integrity. In the event of DNA damage, p53 regulates the transcription of genes that lead to apoptosis or cell-cycle arrest (Polyak *et al.*, 1997; Kastan *et al.*, 1991). The p53 protein has four domains: an amino-terminal transactivation domain (residues 1–44), a core DNA-binding domain (102–292), a tetramerization domain (residues 320–356) and a carboxyl-terminal regulatory domain (residues 320–356). Greater than 50% of human cancers are associated with mutations to p53 and an estimated 95% of all tumorogenic mutations map to the region of the p53 gene that encodes the core domain (Bullock & Fersht, 2001; Levine, 1997). The missense mutations that occur in this region have been classified into two groups: mutations that directly disrupt p53–DNA contacts and mutations that decrease the thermal stability of the core domain.

Owing to the crucial role that the core domain plays in the function of p53, it presents a potentially valuable therapeutic

Table 1
Data-collection and refinement statistics.

	High resolution	2-Propanol soak	HEPES
Space group	*C*2	*C*2	*C*2
Unit-cell parameters			
a (Å)	92.34	92.30	91.57
b (Å)	44.53	44.54	44.71
c (Å)	63.02	62.91	62.61
β (°)	126.25	126.23	125.62
Resolution (Å)	30–1.55	50–2.0	50–2.0
No. of observations	154271	57269	63041
No. of unique reflections	30053	13740	13086
Resolution range (Å)	30.0–1.55	50–2.0	50–2.02
Completeness (%)	97.4 (99.1)	96.2 (87.4)	96.1 (91.9)
$I/\sigma(I)$	31.5 (11.7)	21.1 (3.92)	25.8 (5.82)
$R_{\rm merge}$†	0.040 (0.128)	0.063 (0.263)	0.044 (0.198)
No. of protein atoms	1470	1470	1470
No. of water atoms	256	159	176
No. of Zn atoms	1	1	1
No. of Tris atoms	8	8	0
R factor‡ (%)	18.37	20.89	21.00
$R_{\rm free}$§ (%)	22.78	24.65	22.47
Mean *B* value (Å^2)	20.44	29.43	33.09
R.m.s.d. bonds (Å)	0.010	0.011	0.006
R.m.s.d. angles (°)	2.20	1.44	1.33
Dihedral angles (°)	27.3	26.2	25.4
Improper angles (°)	1.37	0.84	0.88

† $R_{\rm merge} = \sum_h \sum_j |I_{h,j} - \langle I_h\rangle| / \sum_h \sum_i I_{h,j}$, where $\langle I_h\rangle$ is the mean intensity of symmetry-related reflections. ‡ *R* factor = $\sum ||F_{\rm o}| - |F_{\rm c}|| / \sum |F_{\rm o}|$, where $F_{\rm o}$ and $F_{\rm c}$ are the observed and calculated structure-factor amplitudes, respectively. § $R_{\rm free}$ is calculated for 5% of the data that was withheld from refinement.

target. Indeed, a significant number of studies have addressed the feasibility of restoring function in tumor-derived p53 core-domain mutants. In the case of DNA-contact mutants, introduction of amino-acid residues that make additional contacts to DNA have been shown to rescue the function of these mutants (Wieczorek *et al.*, 1996). In the case of mutations that reduce the thermostability of the core domain, second-site mutations have been identified which stabilize common tumor-derived p53 core-domain mutants (Brachmann *et al.*, 1998). These second-site mutations have been shown to mediate thermodynamically favorable interactions that compensate for deleterious mutations located in other regions of the core domain (Nikolova *et al.*, 2000). Together, these studies suggest that the development of small-molecule compounds that compensate for deleterious DNA-contact or protein-stability mutants may provide useful strategies to restore function to common tumor-derived p53 mutant proteins.

Structure-based drug design is a powerful strategy for the development of small-molecule compounds to modulate the function of a protein. Towards this goal, several p53 core-domain structures that might be used for structure-based design have been reported, albeit to medium resolution. The X-ray crystal structure of the human core domain in complex with DNA (Cho *et al.*, 1994) and the mouse core domain without DNA (Zhao *et al.*, 2001) have been reported to resolutions of 2.2 and 2.7 Å, respectively. In addition, the structures of several superstable human p53 core-domain mutants have been determined (Joerger *et al.*, 2004, 2005) with resolution ranging from 1.98 to 1.80 Å. Although these structures provided important insights into several aspects of p53 function, the moderate resolution of these structures limits their usefulness in rational drug-design strategies.

In an attempt to prepare a very high resolution p53 core-domain structure that is more amenable to structure-based drug design, we crystallized the mouse p53 core domain and identified a new crystallization condition that produces crystals that diffract to 1.55 Å resolution and we report its refined structure here. Unexpectedly, the structure reveals a bound buffer molecule of tris(hydroxymethyl)aminomethane (Tris) and interestingly this Tris molecule mediates multiple hydrogen bonds to a region of p53 shown to be important for the repair of a subset of tumor-derived p53 mutations. Based on this observation, we performed equilibrium denaturation experiments and molecular-dynamics simulations in the presence and absence of Tris and the results are consistent with increased thermodynamic stability of the p53 core domain in the presence of Tris. We also show that these crystals of the p53 core domain are suitable for the multiple-solvent crystal structure approach to identify other potential binding sites for possible core-domain stabilization. Finally, we carried out an analysis of local regions of disorder within the mouse p53 core domain to provide insights into areas of conformational flexibility that might be appropriate sites for the binding of other p53-stabilizing compounds. Together, these studies provide a molecular scaffold for the structure-based design of p53-stabilization compounds for development as possible therapeutic agents.

2. Experimental procedures

2.1. Protein purification and crystallization

The mouse p53 core domain was purified as described elsewhere (Zhao *et al.*, 2001). Briefly, the pRSETA (Invitrogen) bacterial expression vector encoding the p53 mouse core domain (residues 92–292) was overexpressed in *Escherichia coli* BL21(DE3) induced with 0.5 m*M* isopropyl 1-thio-β-D-galactopyranoside (IPTG) at a growth temperature of 288 K. The protein was purified using a combination of cation-exchange (SP-Sepharose) and gel-filtration (Superdex-75) chromatography in a buffer containing 20 m*M* sodium citrate pH 6.1, 100 m*M* NaCl, 10 μ*M* zinc acetate and 1 m*M* TCEP. The protein was concentrated to $\sim$10 mg ml^{-1} using filtration by centrifugation and frozen at 193 K for storage prior to crystallization. Crystals were obtained by the hanging-drop method by mixing protein and reservoir solutions in a 1:1 ratio and equilibrating against a reservoir solution containing 100 m*M* Tris pH 7.0 and 16–18% PEG 2K MME (monomethylether) at 293 K. Crystals appeared overnight and grew to typical dimensions of 0.3 $\times$ 0.1 $\times$ 0.1 mm in 2–3 d. Crystals were flash-frozen in 100 m*M* Tris pH 7.0, 20% PEG 2K MME and 20% MPD.

2.2. Data collection, structure determination and refinement

Two data sets were collected at 120 K at the 19BM beamline at the Advanced Photon Source, Argonne National Labora-

tory using a Quantum CCD detector. A high-resolution data set was collected at a crystal-to-detector distance of 120 mm. In order to avoid overloads in the low-resolution bins, a low-resolution data set was collected at a crystal-to-detector distance of 240 mm with a shorter exposure time using the same crystal. Crystals form in space group *C*2, with one molecule per asymmetric unit, and diffract strongly to 1.55 Å resolution (Table 1). Data were processed with *HKL*-2000 and the structure was solved by molecular replacement with the program *AMoRe* (Navaza, 1994) using data from 27 to 3.0 Å resolution with the 1hu8 structure as a search model. Rotation and translation searches followed by rigid-body refinement yielded an unambiguous solution with an *R* factor of 35.9% and a correlation-coefficient value of 69.4%. The protein model was initially refined automatically using data from 7 to 1.55 Å resolution with the programs *ARP*/*wARP* and *guiSIDE* (Perrakis *et al.*, 1999; Perrakis *et al.*, 2001) and manual adjustments were carried out with the program *O* (Jones *et al.*, 1991). Simulated-annealing molecular dynamics was performed using *CNS* (Brünger *et al.*, 1998). As the refinement of atomic position reached convergence, isotropic *B* factors were refined and water molecules were added using the waterpick routine of *CNS*. The data was then extended to 30–1.55 Å resolution and a bulk-solvent correction was added. *SHELX*97 was used for further refinement (Sheldrick & Schneider, 1997) against *F* and the same $R_{\rm free}$ set was used throughout the refinement. The model was subjected to a stepwise increase in resolution (STIR) from 3.0 to 1.55 Å using 0.005 Å increments, resulting in $R_{\rm working}$ and $R_{\rm free}$ of 21.14 and 26.01%, respectively. Anisotropic displacement parameter refinement was then introduced (ANIS) and the model was refined for another 30 rounds. This resulted in a dramatic drop in the $R_{\rm working}$ and $R_{\rm free}$ parameters to 18.83 and 22.90%, respectively. The resulting electron-density maps were considerably improved. At this point, clear electron density could be observed for a molecule of tris(hydroxymethyl)-aminomethane (Tris), which was in the crystallization buffer. Tris was then appropriately built using the program *O* and refined using *SHELX*97, resulting in a final model with $R_{\rm working}$ and $R_{\rm free}$ parameters of 18.37 and 22.78%, respectively. The final model has excellent stereochemistry (Table 1), with 89.1% (139 total) of the residues in the most favorable regions and 10.9% (17 total) in additional allowed regions of the Ramachandran plot.

p53 core-domain crystals for 2-propanol-soaking experiments were harvested in 100 m*M* Tris pH 7.0, 20% PEG 2K MME and soaked in 100 m*M* Tris pH 7.0, 20% PEG 2K MME, 35% 2-propanol for at least 6 h. Crystals were looped and frozen directly in liquid propane. Data collection was carried out on a Rigaku R-AXIS IV detector with a rotating copper-anode generator. Crystals diffracted to a maximum of 2.0 Å. $F_{\rm o,\ 2\text{-}propanol} - F_{\rm o,\ native}$, $F_{\rm o,\ native} - F_{\rm o,\ 2\text{-}propanol}$, $F_{\rm o,\ 2\text{-}propanol} - F_{\rm c,\ 2\text{-}propanol}$ and $2F_{\rm o} - F_{\rm c}$ maps were generated using the previously solved native structure with all waters removed. Assignment of potential 2-propanol density was based on careful examination of electron density at various σ levels in conjunction with plausible functional group interactions. After addition of waters, the structure was refined to final $R_{\rm factor}$ and $R_{\rm free}$ parameters of 20.89 and 24.65%, respectively.

Mouse p53 core-domain crystals grown in the absence of Tris were obtained from conditions similar to the Tris-bound crystals except for the substitution of 100 m*M* HEPES pH 7.0 for 100 m*M* Tris pH 7.0. Crystals appeared to be isomorphous to those obtained using Tris buffer and were frozen using the same cryoprotectant conditions. Data were collected at the Advanced Photon Source, Argonne National Laboratory. Crystals diffracted to a maximum of 2.02 Å. The unit-cell parameters were nearly identical to those of the crystals obtained with Tris buffer and the model was built using the previously solved structure with waters removed as a starting structure. All structural figures were rendered using *PyMOL* unless otherwise noted (DeLano, 2002).

2.3. Equilibrium denaturation

Protein was diluted from concentrated aliquots to 10 µ*M* using premade stocks of buffer consisting of either buffers *A*, *B*, *C* or *D*. Buffer *A* contained 50 m*M* phosphate pH 6.4, 100 m*M* NaCl and 1 m*M* TCEP. Buffer *B* contained 50 m*M* phosphate pH 6.4, 100 m*M* NaCl, 1 m*M* TCEP in addition to 8 *M* urea. Buffers *C* and *D* were identical to buffers *A* and *B*, respectively, except for the presence of 1 m*M* Tris–HCl. Measurements were taken on a PTI spectrofluorimeter (Photon Technologies International, Birmingham, NJ, USA) equipped with an LPS-220B lamp power supply, MD-5020 motor driver and SC-500 shutter control and operated using the *Felix* software package. The temperature was maintained at 283 K using a water bath. Typically, 800 µl of 10 µ*M* protein dissolved in buffer *A* or *C* was placed in a quartz cuvette with a 5 mm path length (Starna Cells, Atascadero, CA, USA). An excitation wavelength of 280 nm (4 nm bandpass) was used and a spectrum was then recorded from 300 to 400 nm (4 nm bandpass). Fully unfolded protein (8 *M* urea) was observed to have a fluorescence maximum at 350 nm. After each reading, 20 µl of the protein solution in the cuvette was removed and replaced with 20 µl of protein dissolved in either buffer *B* or *D* and then stirred using a magnetic stirrer. The pH (6.4) of urea solutions at $U_{50\%}$ in the presence or absence of Tris was identical. Unfolding of the mouse p53 core domain in urea was reversible as evidenced by the observation of a similar spectrum to folded protein upon dilution of the protein from 8 *M* urea. After normalization, the data were fitted to a two-state equation (Bullock *et al.*, 1997),

$$F = \frac{(\alpha_N + \beta_N[D]) + (\alpha_D + \beta_D[D])\exp\{m([D] - [D]_{50\%})/RT\}}{1 + \exp\{m([D] - [D]_{50\%})/RT\}}$$

using the *Origin* software package (Microcal, Northhampton, MA, USA), where *F* is the fluorescence at 350 nm, α_N and α_D are the intercepts at fully folded and unfolded conditions, respectively, β_N and β_D are the slopes at fully folded and unfolded conditions, $[D]$ is the concentration of urea and $[D]_{50\%}$ is the concentration of urea at the point of inflection, with m being the slope of that transition. $\Delta\Delta G$ for Tris and protein or protein alone were calculated using the formula

$\Delta\Delta G = \langle m \rangle (D_{\text{Tris, 50\%}} - D_{\text{protein alone, 50\%}})$ (Bullock *et al.*, 1997) with $\langle m \rangle$ values calculated as the average m values of the two data sets (-2.41 ± 0.12 and -2.20 ± 0.08, respectively).

2.4. Molecular-dynamics simulation

Initial coordinates for the p53–Tris complex and p53 (Tris removed from the p53–Tris complex) were taken from the high-resolution crystal structures. All molecular-dynamics (MD) simulations were performed using the parallelized MD program *GROMACS* 3.3 with constant number, pressure and temperature (NPT) and periodic boundary conditions (Stryer, 1988; Kabsch & Sander, 1983; Mierke & Kessler, 1991). Before MD simulations, explicit polar and aromatic H atoms were added for both models. The GROMOS96 force field was used for the proteins. The topology file and other force-field parameters of Tris were generated using the *PRODRG* program (Schüttelkopf & van Aalten, 2004).

Both the p53–Tris complex and p53 were solvated in a rectangular periodic box filled with SPC water molecules (Berendsen *et al.*, 1981). The minimum distance between the protein atoms and the box walls was set to be >10 Å. Counterions were added to neutralize the net charges of the systems and each system was subjected to energy minimization using the steepest-descent method until the energy convergence at 100 kJ mol^{-1} nm^{-1}. Afterwards, each system was equilibrated for 200 ps. Finally, a 5 ns MD simulation was performed on each system. The linear constraint solver (LINCS) method (Hess *et al.*, 1997) was used to constrain bond lengths, allowing an integration step of 2 fs. Electrostatic interactions were calculated with the Particle-Mesh Ewald algorithm (Darden *et al.*, 1993; Essmann *et al.*, 1995). A constant pressure of 10^5 Pa was applied with a coupling constant of 1.0 ps. The Particle-Mesh Ewald (PME) method was used to calculate electrostatic interactions. The simulated systems were coupled into an external temperature bath at 300 K with a coupling constant of 0.1 ps and isotropic pressure coupling with time constant of 1 ps was applied to keep the pressure at 10^5 Pa. The structures for analysis were saved every 500 steps (1 ps). MD simulations were run on Pittsburgh Supercomputing Center using Linux servers. Analyses were performed using facilities within the *GROMACS* package.

3. Results

3.1. Overall structure of the mouse p53 core domain

The crystal structure of the mouse p53 core domain was determined to 1.55 Å in space group $C2$ and represents the highest resolution structure of the core domain to date. The

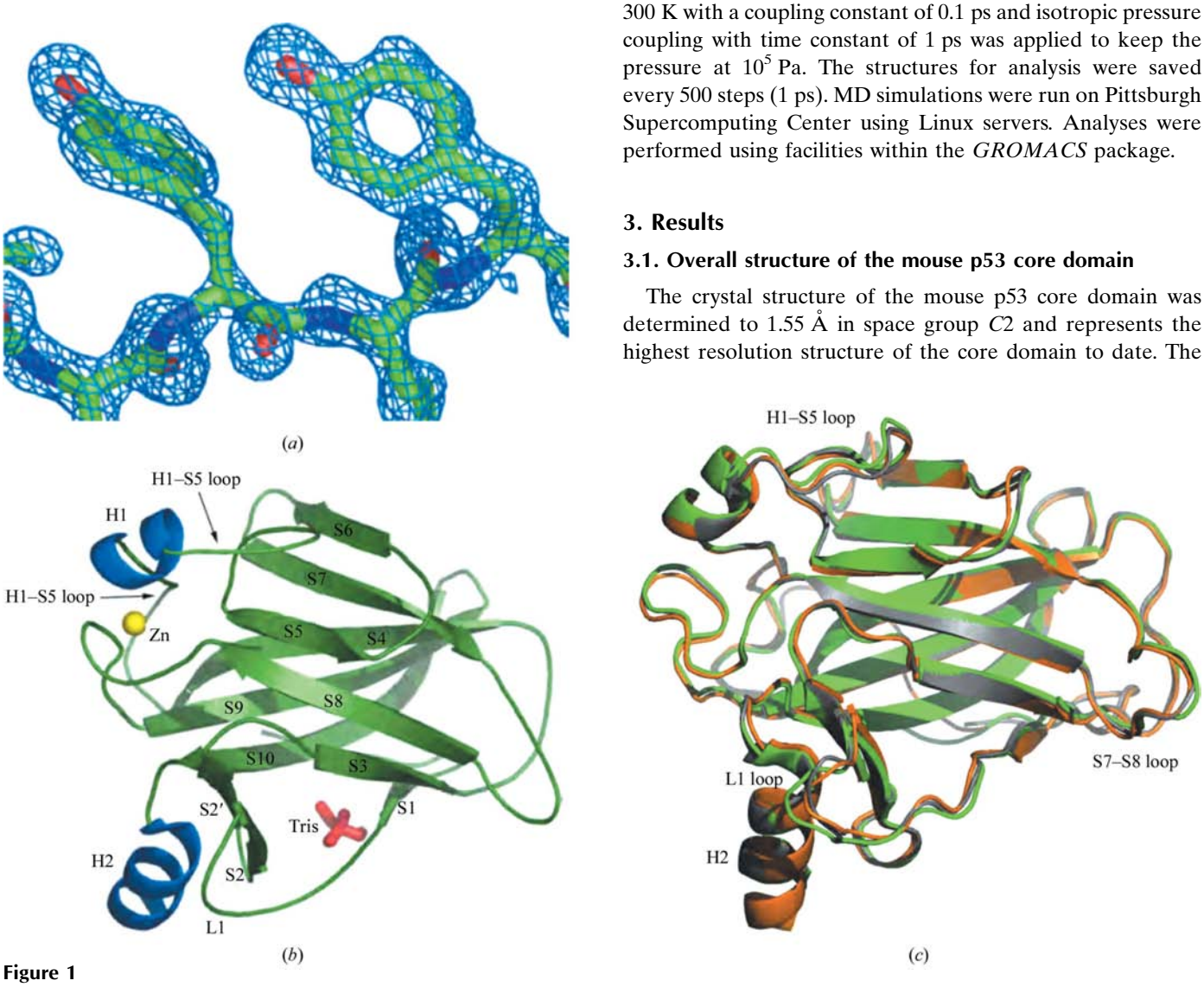

Figure 1
Overall structure of the mouse p53 core domain. (*a*) Representative $F_o - F_c$ OMIT electron-density map of residues 231–233 contoured at 3.5σ. (*b*) Overall structure of the mouse p53 core domain solved to 1.55 Å resolution. The Zn atom is shown as a yellow sphere and a molecule of Tris is shown in red. (*c*) Overlay of the mouse core domain solved at 1.55 Å resolution in space group $C2$ (HR, green), the mouse p53 core domain solved at 2.7 Å in space group $C222_1$ (PDB code 1hu8, grey) and the human p53 core domain unbound to DNA (PDB code 1tsr; orange)

p53 core domain crystallizes as a monomer and contains one molecule per asymmetric unit. The electron-density map is of excellent quality (Fig. 1*a*), with virtually all of the main chain and a majority of the side chains, including surface lysine and methionine residues, which are typically disordered, modeled unambiguously using $2F_o - F_c$ and $F_o - F_c$ electron density.

The overall fold of the high-resolution mouse p53 core domain (Fig. 1*b*) is similar to that previously reported for other p53 core-domain structures at lower resolution (Zhao *et al.*, 2001; Cho *et al.*, 1994; PDB codes 1hu8 and 1tsr, respectively). Briefly, the core domain forms two regions of twisted antiparallel sheets (S1, S3, S5, S8 and S6, S7, S4, S9, S10). In

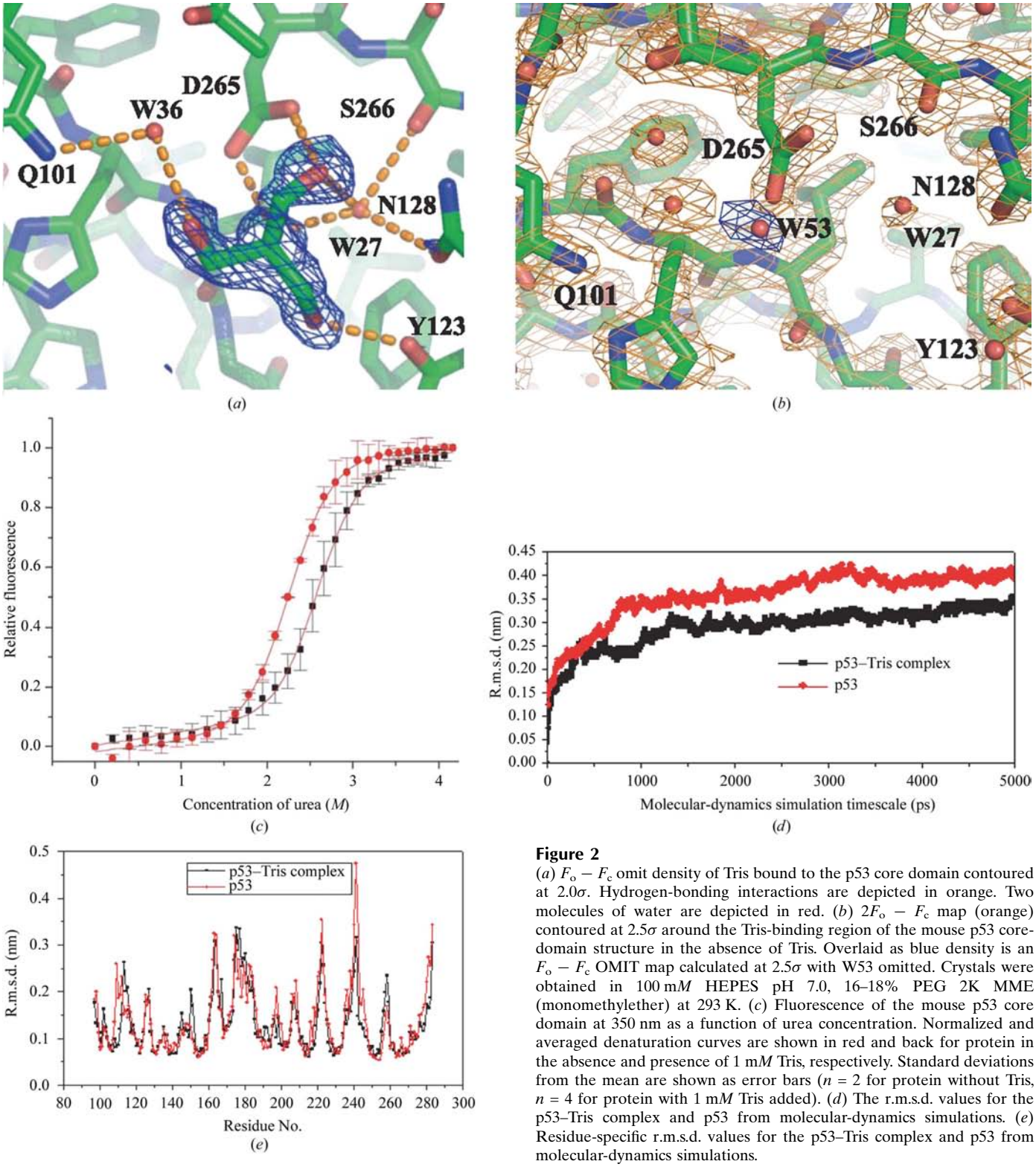

Figure 2
(*a*) $F_o - F_c$ omit density of Tris bound to the p53 core domain contoured at 2.0σ. Hydrogen-bonding interactions are depicted in orange. Two molecules of water are depicted in red. (*b*) $2F_o - F_c$ map (orange) contoured at 2.5σ around the Tris-binding region of the mouse p53 core-domain structure in the absence of Tris. Overlaid as blue density is an $F_o - F_c$ OMIT map calculated at 2.5σ with W53 omitted. Crystals were obtained in 100 m*M* HEPES pH 7.0, 16–18% PEG 2K MME (monomethylether) at 293 K. (*c*) Fluorescence of the mouse p53 core domain at 350 nm as a function of urea concentration. Normalized and averaged denaturation curves are shown in red and back for protein in the absence and presence of 1 m*M* Tris, respectively. Standard deviations from the mean are shown as error bars (n = 2 for protein without Tris, n = 4 for protein with 1 m*M* Tris added). (*d*) The r.m.s.d. values for the p53–Tris complex and p53 from molecular-dynamics simulations. (*e*) Residue-specific r.m.s.d. values for the p53–Tris complex and p53 from molecular-dynamics simulations.

addition, there are two α-helices: one at the C-terminal end of the molecule (H2) and another shorter helix (H1) near a site for zinc chelation. A structural Zn atom is coordinated by four residues: cysteines 238, 242 and 176 and histidine 179 (human numbering). Also included in the high-resolution structure is a well ordered Tris buffer molecule that is bound on the protein surface between the S1 and S10 strands (Fig. 1*b*).

3.2. Comparison with other p53 core-domain structures

The high-resolution mouse p53 core-domain structure in space group *C*2 (HR) superimposes well with the 2.7 Å structure of the mouse p53 core domain in space group $C222_1$ (PDB code 1hu8) and both the DNA-bound and unbound forms (chains *B* and *A* of PDB code 1tsr) of the 2.2 Å human p53 core-domain structure (Cho *et al.*, 1994). A superposition of the structures reveals r.m.s. deviation values of 0.447, 0.753 and 0.670 Å for C^{α} atoms, respectively. Not surprisingly, the central β-sheet-rich core region shows the greatest structural superposition, while the surrounding loops show the greatest divergence. Specifically, the L1 (between the S1 and S2 strands) and H1–S5 loops show the greatest structural divergence. This result highlights the high degree of structural conservation between the core domains of p53 from different species and reveals that DNA-specific binding does not involve significant protein structural rearrangement, which is consistent with previous proposals (Zhao *et al.*, 2001).

A comparison of the DNA-bound form with HR reveals that while the H2 helix, jointly responsible for DNA binding with the L1 loop, remains essentially unchanged, the L1 loop undergoes a larger structural shift between the two proteins (Fig. 1*c*). This result was not surprising since the L1 loop is apparently flexible as revealed by comparison of several p53 core-domain crystal structures (PDB codes 2bin, 2bio, 2bip, 2biq, 2geq). Additionally, residues 178–186 of the mouse p53 core domain, corresponding to the H1–S5 loop, shows a C^{α} r.m.s. deviation of 0.438 Å when compared with the lower resolution mouse p53 core domain (PDB code 1hu8). The 1hu8 structure implicates the H1–S5 loop of one p53 core domain in mediating dimerization contacts *via* interactions with the S4–H1 (L2) and S6–S7 loops of another p53 core domain (Zhao *et al.*, 2001). This interaction maintains p53 in a configuration that is incompatible with simultaneous DNA binding by both protomers of the dimer. In HR, the H1–S5 loop is also involved in intersubunit crystal contacts, but with the S5–S6 loop. This comparison suggests that the flexibility of the H1–S5 loop could play an important role in p53 function *via* intersubunit core-domain interactions.

3.3. Location and characterization of a Tris molecule in the core-domain structure

A molecule of Tris was observed in the electron-density map of HR during refinement of the model. The electron density for this molecule is very well defined and the average thermal factor for the Tris atoms is 32.50 $Å^2$, which is within the average range for thermal factors for the HR structure. The Tris molecule binds between the S1 and S10 strands of the protein and makes direct and water-mediated hydrogen-bonding interactions with the side-chain atoms of residues Tyr123, Asn128 and Asp265 (Fig. 2*a*). Additionally, the Tris molecule makes water-mediated hydrogen-bonding interactions to the backbone carbonyl of Ser266 and to the side-chain N atom of Gln101. Interestingly, the location of the bound Tris molecule is close to the position of the human N268D stabilization mutation and appears to play a similar role in introducing bridging interactions between the S1 and S10 strands of the p53 core domain.

To further assess the structural significance of the Tris-mediated p53 interaction, we prepared isomorphous crystals of the mouse p53 core domain in which HEPES buffer was used in place of Tris buffer and we determined the structure to 2.0 Å resolution (Table 1). The structure of the p53 core domain in the presence of HEPES buffer reveals that one water molecule (W53) overlaps a region of electron density that had been occupied by Tris and each of the two water molecules that had bridged Tris–p53 interactions (W27 and W36) are also present (Fig. 2*b*). Notably, however, W53 does not appear to compensate for the Tris-mediated intra-protein interactions.

Although attempts to observe direct binding of Tris to the p53 core domain in solution using ITC (isothermal titration calorimetry) were unsuccessful (RM and WCH, unpublished data), presumably owing to the weak binding affinity of Tris for the p53 core domain, we tried to test directly whether high concentrations of Tris (1 m*M*) could stabilize the p53 core domain by carrying out chemical denaturation experiments of the p53 core domain in the presence or absence of Tris. For these studies, the mouse p53 core domain was subjected to urea equilibrium denaturation experiments in the presence or absence of 1 m*M* Tris. Unfolding was monitored by measuring fluorescence of a single buried tryptophan, which increased in fluorescence to a maximum of λ = 350 nm as unfolding proceeded. These experiments revealed that in the presence of 1 m*M* Tris, the mouse p53 core domain has a $U_{50\%}$ (concentration of urea required for 50% unfolding) of 2.58 ± 0.02 *M*, compared with 2.20 ± 0.08 *M* for protein in the absence of Tris (Fig. 2*c*). Analysis of this data yields a $\Delta\Delta G$ of 3.1 kJ mol^{-1} for Tris binding.

3.4. Molecular-dynamic simulations of the p53 core domain in the absence and presence of bound Tris

The behavior of the p53–Tris complex and p53 alone was studied by molecular-dynamics simulation to account for protein flexibility within a simulated solution environment. The starting structures extracted from the p53 and p53–Tris crystal structures reported here were subjected to 5.0 ns MD simulations and the r.m.s.d. values of backbone atoms from their initial positions (t = 0 ps) were used to measure core-domain stability and to gain insight into possible structural fluctuation. The time evolution of the backbone r.m.s.d. values of p53 core-domain atoms for both systems is presented in Fig. 2(*d*). In the plot, a sharp rise in r.m.s.d. was observed during the first 200 ps for all residues and was followed by a

relative flattening out of these fluctuations. However, the magnitude of these r.m.s.d. curves does not continue to increase after about a 1.5 ns MD simulation, implying that both systems are stable over this timescale. The average r.m.s.d. values are about 3.0 and 3.7 Å, respectively, for the p53 core domain in the presence and absence of bound Tris. Interestingly, the reduced r.m.s.d. values in the presence of Tris are not localized but are distributed throughout the p53 core-domain structure (Fig. 2*e*).

3.5. Multiple-solvent crystal structure analysis using p53 core-domain crystals

Although we had fortuitously discovered Tris to be a p53-stabilizing compound, a more systematic approach for determining possible binding sites on the surface of a protein which can potentially be targeted by small molecules is to soak high concentrations of organic solvents into the crystal lattice and locate them in high-resolution electron-density maps (English *et al.*, 1999, 2001; Mattos & Ringe, 1996). Common solvents used for this purpose include 2-propanol, phenol, dioxane, hexane, acetonitrile and acetone, all of which represent probes for varying functional groups. The well diffracting HR crystals of the mouse p53 core domain were suitable for this technique. Using this strategy, we soaked the HR crystals individually with the compounds phenol, 2-propanol, acetonitrile and acetone. Of the molecules tested, soaking p53 crystals in 35% 2-propanol for 6 h produced crystals that did not show compromised diffraction properties and upon structure determination revealed the presence of a 2-propanol-binding site within the core domain (Fig. 3*a*). Specifically, after data collection and examination of the electron density using a combination of $F_{o,\ 2\text{-propanol}} - F_{o,\ native}$, $F_{o,\ 2\text{-propanol}} - F_{c,\ 2\text{-propanol}}$ and $2F_o - F_c$ maps, we located one 2-propanol-binding site near the L1 loop of the protein and bridging interactions between the S1 and S3 β-sheets. OMIT maps of the final structure with the 2-propanol omitted were generated to confirm the presence of the 2-propanol molecule (Fig. 3*b*).

A high-resolution view of the interactions made between 2-propanol and the p53 core domain reveals that the hydroxyl group of the 2-propanol hydrogen bonds to the backbone carbonyl of Pro139 and the backbone amide N atom of Leu111. Analysis of $F_{o,\ 2\text{-propanol}} - F_{o,\ native}$ as well as $F_{o,\ native} - F_{o,\ 2\text{-propanol}}$ difference density at the 2-propanol-binding site reveals several water molecules that are displaced and an altered hydrogen-bonding network in order to accommodate the 2-propanol molecule. Difference density also shows that the sulfur of Cys121 also shifts conformations to accommodate the 2-propanol. The bottom of this pocket is lined with hydrophobic residues, including Phe110, Phe267, Leu130 and Tyr123, which are in a suitable environment to interact with the methylene groups of 2-propanol. A surface plot of the region reveals a depression where the 2-propanol molecule binds (Fig. 3*c*), which, interestingly, is located at a one potential key area of function of the p53 core domain, the L1 loop that can participate in DNA binding. Interestingly, the presence of the 2-propanol compound at the L1 DNA-binding loop suggests that this binding site might provide a useful template for increasing the stability of the p53 core domain and potentially also for introducing additional p53 core domain–DNA contacts that might compensate for tumor-derived p53 mutations that directly disrupt p53–DNA contacts.

3.6. Analysis of local regions of disorder in the mouse p53 core domain

As the data-to-parameter ratio increases at higher resolution, one can begin to examine the regions of disorder of the mouse p53 core domain in detail, which can provide further insight into areas of conformational flexibility that might be targets for p53-stabilizing compounds. To carry out this analysis using the high-resolution mouse p53 core-domain data, isotropic thermal factors (*B* values) and anisotropic

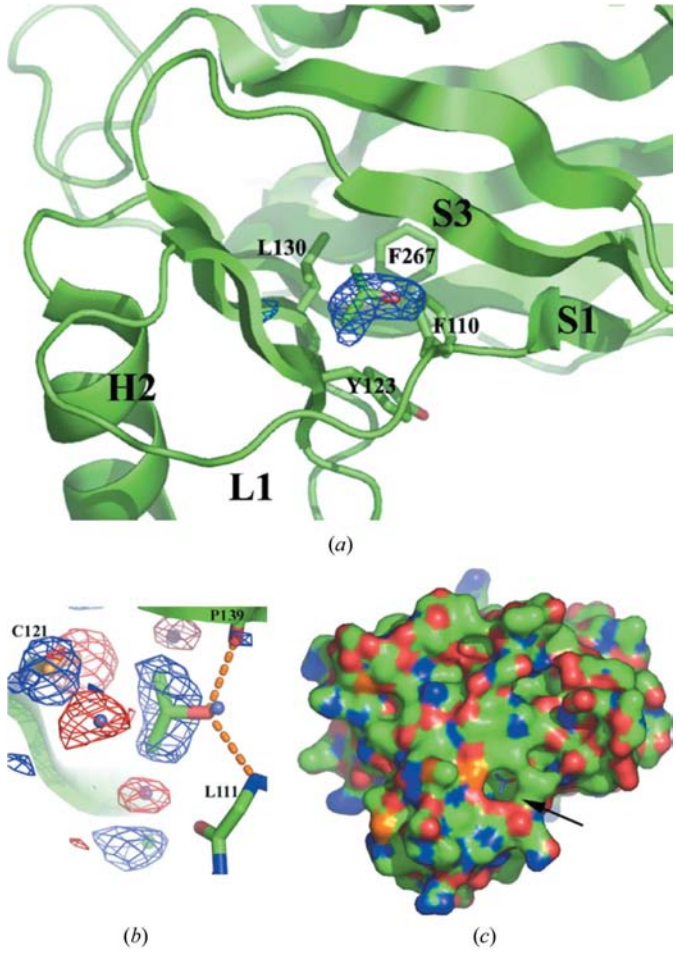

Figure 3
Location of a 2-propanol molecule bound to the mouse p53 core domain. (*a*) Density surrounding the location of the 2-propanol-binding site. Blue density, $F_{o,\ 2\text{-propanol}} - F_{o,\ native}$ at the 2.5σ level. (*b*) $F_o - F_c$ OMIT map calculated at 2.5σ using the final structure with 2-propanol omitted. Red density, $F_{o,\ native} - F_{o,\ 2\text{-propanol}}$; blue spheres, water molecules observed in native structure; green sphere, water observed in 2-propanol-soaked structure; orange dashes, hydrogen bonding. (*c*) Surface representation of the 2-propanol-binding site with 2-propanol shown as a stick figure. The 2-propanol-binding site is denoted by an arrow. C, O and N atoms are colored green, red and blue, respectively.

displacement parameters were refined as the data allowed (Fig. 4*a*). A plot of the average main-chain thermal factors as a function of main-chain atoms reveals that the L1, H1–S5 and S7–S8 loops have the highest thermal factors, consistent with the highest regions of p53 core-domain flexibility as suggested from the comparison between different p53 core domains (Fig. 1*c*).

Residues within the S7–S8 loop display the highest thermal factors in the entire structure (Fig. 4*b*, top panel). Moreover, the main-chain atoms of the S7–S8 loop region also display the highest degree of anisotropy in the entire protein (Fig. 4*b*, bottom panel). These findings suggest that the S7–S8 loop is not only flexible, but also contains a directional component to that flexibility. A plot of the main-chain thermal ellipsoids with a 20% probability sphere reveals a possible concerted 'hinge-like' movement of the S7–S8 loop (Fig. 4*d*). On visual inspection, the anisotropic disorder in the main chain for residues 221, 222, 223 and 224 point in the same direction, possibly creating a hinge that pivots between Pro220 at the N-terminal end and Glu225 at the C-terminal end. Analysis of the Rosenfield matrix shows that residues in the S7–S8 loop do indeed move in a direction independent from the rest of the protein (Fig. 4*c*). The high degree of sequence conservation among p53 proteins in the S7–S8 loop suggests that this hinge-like motion may have a functional consequence, which may be to facilitate intersubunit contacts. This result is supported by our recent modeling of a tetrameric complex from the structure of dimeric mouse p53 core domain bound to DNA (Ho *et al.*, 2006). In this model, we predict that in the tetrameric form the S7–S8 and L2 loops of the p53 core domain are likely to make tail–tail interactions when bound to DNA.

The L1 loop, which can be involved in DNA binding, shows the greatest degree of core-domain variability as determined by the elevated thermal factors calculated for this region and as determined by comparison to the other p53 core-domain structures (Fig. 1*c*). Interestingly, analysis of the mean anisotropy of this region of the structure reveals that the disorder is more isotropic. Further analysis of thermal ellipsoids supports

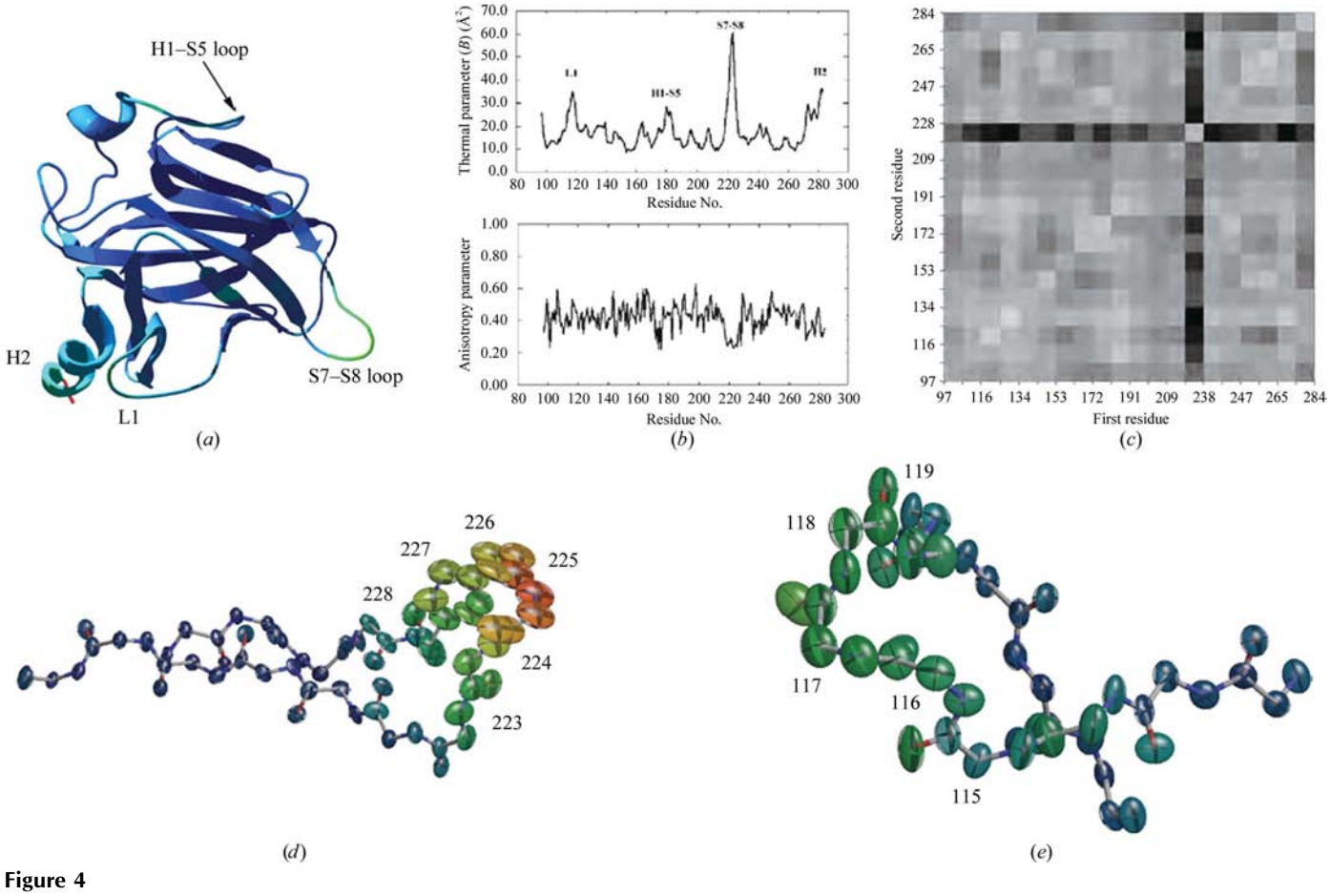

Figure 4
Mobility of the p53 core domain (*a*) Plot of temperature factors (*B*) on the secondary structure of the mouse p53 core domain. Colors represent temperature-factor magnitudes. The highest temperature factors are in red and the lowest are in darker shades of blue. The figure was produced using *SWISS-PDB VIEWER* (Guex & Peitsch, 1997) and then rendered using *POV-Ray*. (*b*) Top, average temperature factor (*B*) of main-chain atoms as a function of residue number; bottom, mean anisotropy of main-chain atoms plotted as a function of residue number. Anisotropy is shown as a ratio of the degree of displacement of the shortest axis to the displacement of the longest axis. The figures were produced using *PARVATI* (Merritt, 1999). (*c*) Rosenfeld matrix generated using the program *ANISOANAL*. Sections of similar shading indicate possible rigid bodies. (*d*) Thermal ellipsoid plot of 20% probability spheres for main-chain atoms in the S7–S8 loop region. Atoms colored blue represent a minimal *B* factor of 10 Å^2; atoms colored red represent a maximum *B* factor of 65 Å^2. The figure was produced using *RASTEP* (Merritt & Bacon, 1997). (*e*) Thermal ellipsoid plot of 20% probability sphere of the L1 region. The figure was produced using *RASTEP* (Merritt & Bacon, 1997).

this (Fig. 4*e*), as many ellipsoids are not as elongated as observed in the case of the S7–S8 loop. The isotropic nature of the disorder suggests that while the L1 loop is very flexible, the flexibility does not favor any particular direction. Analysis of the main-chain thermal factors of the L1 loop from the human p53 core domain–DNA complex reveals thermal factors that are about average for the overall structure (Cho *et al.*, 1994), reinforcing the conclusion that the L1 loop can become ordered upon DNA binding by p53.

4. Discussion

In this study, we report a 1.55 Å resolution structure of the mouse p53 core domain, representing the highest resolution p53 core-domain structure reported to date. A comparison of the high-resolution p53 core-domain structure reported here with other p53 core-domain structures from different species and in different crystal lattices reveals a highly conserved core structure and three surface loops that appear to be particularly flexible. These are the S7–S8, H1–S5 and L1 loops. Although the functional importance of the flexibility of the S7–S8 loop is not yet clear, it appears that the flexibility of the L1 and H1–S5 loops are functionally important. In particular, the H1–S5 loop has been proposed to play a role in modulating the dimerization properties of the p53 core domain for suitable DNA binding and the appropriate conformation of the L1 loop may be important for mediating sequence-specific interactions.

The high-resolution p53 core-domain structure fortuitously uncovered a stabilizing Tris buffer molecule between the S1 and S10 strands of the core domain. Interestingly, two Tris molecules were also found in similar positions in the recently reported dimeric mouse p53–DNA complex (Ho *et al.*, 2006). The Tris molecule makes numerous interactions with the protein that are reminiscent of the stabilizing interactions made by the aspartic acid of a human N268D mutant that restored activity to several tumor-derived p53 mutant proteins (Joerger *et al.*, 2004). Correlating with the significance of the p53–Tris interactions seen in the crystals, equilibrium denaturation experiments demonstrate that Tris increases the thermostability of the p53 core domain by about 3.1 kJ mol^{-1} and molecular-dynamics simulations showed larger r.m.s.d. values when Tris was not bound. To our knowledge, this represents the first identification of a small-molecule (low-molecular-weight) compound that interacts with and increases the thermodynamic stability of p53 and we propose that the p53–Tris complex may provide a useful scaffold for the structure-based design of p53-stabilizing compounds.

The multiple-solvent crystal structure strategy of soaking the crystal lattice with organic solvents was also employed with the solvent 2-propanol, revealing an area of weak affinity located at an area of functional significance as well as considerable flexibility: the L1 loop. The 2-propanol-binding site might also be exploited for the development of compounds that may stabilize the p53 core domain and/or introduce additional p53 core domain–DNA interactions that might compensate for a subset of tumor-derived p53 mutations.

Previous reports have described the preparation of small-molecule compounds that restore p53 function to common tumor-derived p53 mutant proteins. These include a group of acridine molecules (Foster *et al.*, 1999) and PRIMA-1 (Bykov *et al.*, 2002). However, more recent studies have revealed that the acridine molecules do not bind directly to p53 (Rippin *et al.*, 2002). In addition, we have recently found that the PRIMA compound also does not bind directly to p53 (unpublished data) and thus is proposed to promote p53 function indirectly. In contrast to these earlier studies, the studies reported here provide a rational framework for the design and development of small-molecule compounds that could directly target tumor-derived p53 mutant proteins for the treatment of human cancer.

We thank A. Joachimiak, R. Zhang, N. Duke and the SBC-CAT staff for access to and assistance with the 19BM beamline at APS. We would also like to thank G. Van Duyne and G. S. Pesiridis for use of their spectrofluorimeter and for helpful advice. This work was supported by NIH (GM52880) and DOD (W81XWH-04-1-0564) grants to RM, a grant to WCH from the DOD (DAMD17-02-1-0629) and a grant from the Commonwealth Universal Research Enhancement Program, Pennsylvania Department of Health awarded to the Wistar Institute. Use of the Argonne National Laboratory Structural Biology Center beamline at the Advanced Photon Source was supported by the US Department of Energy, Office of Biological and Environmental Research under Contract No. W-31-109-ENG-38.

References

Berendsen, H. J. C., Postma, J. P. M., van Gunsteren, W. F. & Hermans, J. (1981). *Intermolecular Forces*, edited by B. Pullman, pp. 331–342. Dordrecht: Reidel.

Brachmann, R. K., Yu, K., Eby, Y., Pavletich, N. P. & Boeke, J. D. (1998). *EMBO J.* **17**, 1847–1859.

Brünger, A. T., Adams, P. D., Clore, G. M., DeLano, W. L., Gros, P., Grosse-Kunstleve, R. W., Jiang, J.-S., Kuszewski, J., Nilges, M., Pannu, N. S., Read, R. J., Rice, L. M., Simonson, T. & Warren, G. L. (1998). *Acta Cryst.* D**54**, 905–921.

Bullock, A. N. & Fersht, A. R. (2001). *Nature Rev. Cancer*, **1**, 68–76.

Bullock, A. N., Henckel, J., DeDecker, B. S., Johnson, C. M., Nikolova, P. V., Proctor, M. R., Lane, D. P. & Fersht, A. R. (1997). *Proc. Natl Acad. Sci. USA*, **94**, 14338–14342.

Bykov, V. J. N., Issaeva, N., Shilov, A., Hultcrantz, M., Pugacheva, E., Chumakov, P., Bergman, J., Wiman, K. G. & Selivanova, G. (2002). *Nature Med.* **8**, 282–288.

Cho, Y., Gorina, S., Jeffrey, P. D. & Pavletich, N. P. (1994). *Science*, **265**, 346–354.

Darden, T., York, D. & Pedersen, L. (1993). *J. Chem. Phys.* **98**, 10089–10092.

DeLano, W. L. (2002). *The PyMOL Molecular Graphics System.* San Carlos, CA, USA: DeLano Scientific.

English, A. C., Done, S. H., Caves, L. S. D., Groom, C. R. & Hubbard, R. E. (1999). *Proteins*, **37**, 628–640.

English, A. C., Groom, C. R. & Hubbard, R. E. (2001). *Protein Eng.* **14**, 47–59.

Essmann, U., Perera, L., Berkowitz, M. L., Darden, T., Lee, H. & Pedersen, L. G. (1995). *J. Chem. Phys.* **103**, 8577–8593.

Foster, B. A., Coffey, H. A., Morin, M. J. & Rastinejad, F. (1999). *Science*, **286**, 2507–2510.

Guex, N. & Peitsch, M. C. (1997). *Electrophoresis*, **18**, 2714–2723.
Hess, B., Bekker, H., Berendsen, H. & Fraaije, J. (1997). *J. Comput. Chem.* **18**, 1463–1472.
Ho, W., Fitzgerald, M. & Marmorstein, R. (2006). *J. Biol. Chem.* **281**, 20494–20502.
Joerger, A. C., Allen, M. D. & Fersht, A. R. (2004). *J. Biol. Chem.* **279**, 1291–1296.
Joerger, A. C., Ang, H. C., Veprintsev, D. B., Blair, C. M. & Fersht, A. R. (2005). *J. Biol. Chem.* **280**, 16030–16037.
Jones, T. A., Zou, J.-Y., Cowan, S. W. & Kjeldgaard, M. (1991). *Acta Cryst.* A**47**, 110–119.
Kabsch, W. & Sander, C. (1983). *Biopolymers*, **22**, 2577–2637.
Kastan, M. B., Onyekwere, O., Sidransky, D., Vogelstein, B. & Craig, R. W. (1991). *Cancer Res.* **51**, 6304–6311.
Levine, A. J. (1997). *Cell*, **88**, 323–331.
Mattos, C. & Ringe, D. (1996). *Nature Biotechnol.* **14**, 595–599.
Merritt, E. A. (1999). *Acta Cryst.* D**55**, 1109–1117.
Merritt, E. A. & Bacon, D. J. (1997). *Methods Enzymol.* **276**, 505–524.
Mierke, D. F. & Kessler, H. (1991). *J. Am. Chem. Soc.* **113**, 9466–9470.
Navaza, J. (1994). *Acta Cryst.* A**50**, 157–163.
Nikolova, P. V., Wong, K., DeDecker, B., Henckel, J. & Fersht, A. R. (2000). *EMBO J.* **19**, 370–378.
Perrakis, A., Harkiolaki, M., Wilson, K. S. & Lamzin, V. S. (2001). *Acta Cryst.* D**57**, 1445–1450.
Perrakis, A., Morris, R. & Lamzin, V. S. (1999). *Nature Struct. Biol.* **6**, 458–463.
Polyak, K., Xia, Y., Zweier, J. L., Kinzler, K. W. & Vogelstein, B. (1997). *Nature (London)*, **389**, 300–305.
Rippin, T. M., Bykov, V. J. N., Freund, S. M. V., Selivanova, G., Wiman, K. G. & Fersht, A. R. (2002). *Oncogene*, **21**, 2119–2129.
Schüttelkopf, A. W. & van Aalten, D. M. F. (2004). *Acta Cryst.* D**60**, 1355–1363.
Sheldrick, G. M. & Schneider, T. K. (1997). *Methods Enzymol.* **277**, 319–343.
Stryer, L. (1988). *Biochemistry*, 3rd ed., p. 211. New York: W. H. Freeman & Co.
Wieczorek, A. M., Waterman, J. L. F., Waterman, M. J. F. & Halazonetis, T. D. (1996). *Nature Med.* **2**, 1143–1146.
Zhao, K., Chai, X., Johnston, K., Clements, A. & Marmorstein, R. (2001). *J. Biol. Chem.* **276**, 12120–12127.